Epitaxial Growth of Nanostructured Gold Films on Germanium via Galvanic Displacement

Sayed Y. Sayed and Jillian M. Buriak*

National Institute for Nanotechnology and Department of Chemistry, University of Alberta, Edmonton, Alberta, Canada T6G 2G2

ABSTRACT This work focuses on the synthesis and characterization of gold films grown via galvanic displacement on Ge(111) substrates. The synthetic approach uses galvanic displacement, a type of electroless deposition that takes place in an efficient manner under aqueous, room temperature conditions. Investigations involving X-ray diffraction (XRD) and transmission electron microscopy (TEM) techniques were performed to study the crystallinity and orientation of the resulting gold-on-germanium films. A profound effect of HF(aq) concentration was noted, and although the SEM images did not show significant differences in the resulting gold films, a host of X-ray diffraction studies demonstrated that higher concentrations of HF(aq) led to epitaxial gold-on-germanium, whereas in the absence of HF(aq), lower degrees of order (fiber texture) resulted. Cross-sectional nanobeam diffraction analyses of the Au−Ge interface confirmed the epitaxial nature of the gold-on-germanium film. This epitaxial behavior can be attributed to the simultaneous etching of the germanium oxides, formed during the galvanic displacement process, in the presence of HF. High-resolution TEM analyses showed the coincident site lattice (CSL) interface of gold-on-germanium, which results in a small 3.8% lattice mismatch due to the coincidence of four gold lattices with three of germanium.

KEYWORDS: galvanic displacement • gold film • germanium surfaces • electron microscopy • X-ray diffraction • pole figures • rocking curves • heteroepitaxy • fiber texture • coincident site lattice interface.

INTRODUCTION

Integration of metallic nanostructures on semiconductor surfaces is attractive (1) for many potential applications in nanoelectronics (2–4), optoelectronics (5, 6), biomedical sensing (7, 8), and others (9, 10). Control over size and shape of nanostructured metals on semiconductors is considered key for tuning their electrical properties, and for other aspects such as surface plasmon resonance (SPR) and surface-enhanced Raman scattering (SERS), for example (11–22). Moreover, tuning the preferred orientation (texture) of the metallic epilayer is an important factor in integrated circuit performance as a result of the electrical conductivity dependence on interconnect microstructure (e.g., defects, voids, internal stress) (23). An efficient and versatile approach for interfacing metals with semiconductor surfaces is galvanic displacement (24–53), a class of spontaneous redox reactions resulting in the reduction of metal ions by the semiconductor valence band electrons (28, 47). Because the reaction is carried out at room temperature in the absence of an external source of electric current or a chemical reducing agent and with the simplest of apparatus (water, metal ion, substrate in a beaker), it is straightforward to carry out and is less expensive and faster than commonly used metal evaporation (54, 55), and sputtering techniques (5, 56).

In addition to the simplicity of galvanic displacement for producing metallic films on semiconductors, recent work has demonstrated that a higher level of sophistication of these films is possible. For instance, in spite of the fact that the reactions are carried out at room temperature, the growth of gold-on-silicon can be heteroepitaxial on both Si(100) and Si(111), as well as silicon nanowires (49, 51). To contrast, epitaxial formation of evaporated gold on silicon requires ultra high vacuum and annealing conditions (57).

The avoidance of interfacial oxides (dielectrics) between the metal and the semiconductor may be imperative for certain technological applications of metal-semiconductor contacts. For instance, with regards to the construction of epitaxial semiconductor architectures such as nanowires on silicon (50, 58), when the gold nanoparticle catalysts for silicon nanowire VLS growth are prepared via galvanic displacement, a high quantity of epitaxial Si nanowires with neat and sharp crystallographic interfaces are produced. Evaporated gold films, on the other hand, led to only small quantities of epitaxial nanowires, with defects at the silicon nanowire-bulk silicon interface (58, 59). Other important aspects of a well-defined, oxide-free metal-semiconductor junction relate to metal adhesion, low defect densities, and good electrical connectivity (28, 36, 60).

Although most of the galvanic displacement literature has focused upon silicon, there is growing interest in the metallization of germanium for a number of applications. For example, the very high mobility of both electrons and holes and the lower band gap of germanium substrates make the material ideally suited for the formation of high-speed

* Corresponding author. E-mail: jburiak@ualberta.ca.
Received for review August 5, 2010 and accepted October 26, 2010
DOI: 10.1021/am100698w

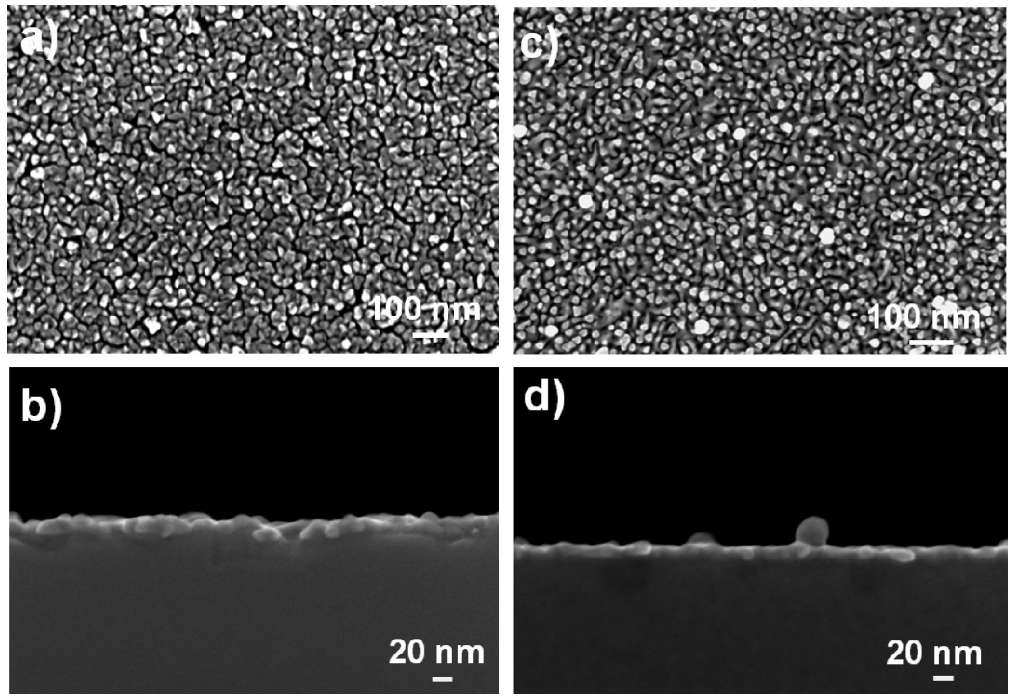

FIGURE 1. Scanning electron micrographs (SEM) for Au films galvanically displaced on Ge(111) after 20 min immersion of germanium shards in solutions containing (a, b) 0.1 mM $KAuCl_4$(aq) and (c, d) 0.1 mM $KAuCl_4$ + 20% HF(aq). (a, c) and (b, d) are plan view and cross-sectional images, respectively.

circuits (61–65). With respect to galvanic displacement, metals-on-germanium have been studied thus far from both a fundamental synthetic perspective, and for applications such as surface enhanced Raman spectroscopy (SERS) (53, 66, 67). Carraro and co-workers showed in 2002 that gold-on-germanium films prepared via a galvanic displacement route result in very well adhering films, and this observation, coupled with XPS evidence, suggested formation of a chemical bond at the interface between the metallic gold and the germanium (29). To date, however, there is little new information relating to the nature of this chemical bonding, whether there is perhaps heteroepitaxial film formation, or the presence of intermetallics, both of which are observed in the gold-on-silicon case. Studies focused upon the oxidation of hydrogen terminated germanium in water has shown evidence for the simultaneous formation and dissolution of GeO_2, leaving GeO_x ($x < 2$) covering the surface (68); in the presence of HF(aq), however, both oxides are soluble (69, 70). To the best of our knowledge, the effects of an oxide etching agent such as HF(aq) on galvanic displacement reactions that lead to direct contact between gold-on-germanium have not been fully explored. In this work, we carry out detailed X-ray diffraction measurements and cross-sectional transmission electron microscopic (TEM) analyses to identify the nature of the gold-on-germanium interface, and demonstrate that under certain conditions, the films are heteroepitaxial.

EXPERIMENTAL SECTION

Generalities. Unless otherwise noted, all experiments were performed under ambient laboratory conditions. Ge(111) (p-type, Ga-doped, $\rho = 0.24-0.33\ \Omega$ cm, 500 μm thickness) wafers were purchased from MTI Corporation. $KAuCl_4 \cdot xH_2O$ were purchased from Strem Chemicals.

Pretreatment of Germanium Substrates. All wafers were diced into 0.8 cm^2 pieces with a diamond scriber. Germanium shards were degreased in a methanol ultrasonic bath for 15 min, in boiling dichloromethane for 10 min, and then a methanol ultrasound bath for 10 min. The oxide layer was removed with a solution of $NH_4OH:H_2O$ (1:4) for 5 min (71, 72). After the oxide etching step, the wafers were rinsed with DI water and dried with a stream of nitrogen.

Metal Deposition. Germanium shards were immersed in either the desired aqueous gold salt solutions or the metallic salt and different concentrations of hydrofluoric acid (HF) in a Teflon beaker. HF concentrations are expressed as weight percent. All of the deposition/immersion reactions were carried out for 20 min in laboratory ambient. After metal deposition, the sample was thoroughly rinsed with water and dried under a nitrogen stream.

Surface Characterization. The gold nanostructures on the germanium surfaces were characterized by scanning electron microscopy (SEM), transmission electron microscopy (TEM), and X-ray diffraction (XRD). SEM (Hitachi S-4800 FE-SEM) images of metallic nanostructures were typically performed with electron energy of 20 keV. High-resolution TEM (HRTEM) images and nanobeam diffraction (NBD) patterns (with a probe of ~5 nm) were recorded on a Shottky-emission 200 kV JEOL 2200FS TEM/STEM microscope with in-column energy filter equipped with a high tilt cryo-polepiece, and a cold-field-emission 300 kV Hitachi HF3300 TEM/STEM microscope with a postcolumn energy filter. The crystalline nature of the metallic upper layer was analyzed by X-ray diffraction (XRD). The out of plane orientation, the theta (θ)−2theta (2θ) scan, was investigated using a Bruker D8 Discover diffractometer equipped with a 1/4 Eulerian cradle, Cu X-ray tube, a 1 mm collimator, and a 2D Hi-Star proportional detector. The detector was placed 15 cm from the sample. The texture of the films and the in plane orientation were investigated using XRD pole figure analyses. To capture the whole (111) pole figure intensity distribution, we tilted the sample at different Ψ angles: 90, 60, 19.5° [$\chi = 90° - \Psi$ (Figure 2)]. At each tilting angle, the sample was rotated azimuthally from $\Phi = 0-360°$ with a 5° scan step (72 frames

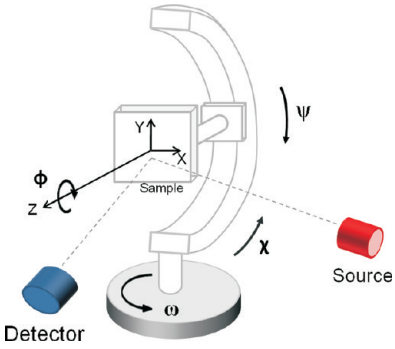

FIGURE 2. Schematic diagram showing the experimental set up used in the in- and out-of-plane orientation analyses by X-ray diffraction. The pole figure was constructed by rotating the sample 360° along the azimuthal axis Φ at different χ angles ($\chi = 90° - \Psi$). The sample was aligned vertically as shown in the figure at $\Psi = 90°$ ($\chi = 0°$). The rocking curves were measured by fixing the detector position at the required 2θ and rocking the sample along the ω axis.

Scheme 1. The Galvanic Displacement Process

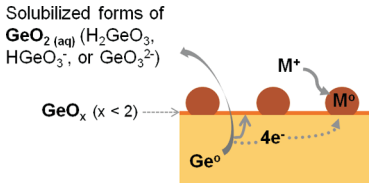

for each Ψ, Figure 2). The out-of-plane mosaicity was evaluated from rocking curves by fixing the detector position at the required 2θ and rocking the sample along the ω axis (Figure 2). The rocking curves were measured using scintillation counter detector.

TEM Sample Preparation on FIB. Cross-sectional TEM samples of Au/Ge(111) were prepared on a Hitachi NB5000 Focused Ion & Electron Beam System. A 40 keV Ga ion beam was used to produce a thin section about 200 nm thick, and Ar ion milling was then used for final thinning and cleaning of the surface. Ion milling was done at low temperature (with LN2 cooling) at a 6° milling angle, and with a two-step process: voltage/current of 1 kV/3 mA for thinning and 0.5 kV/3 mA for final polishing.

RESULTS AND DISCUSSION

The synthesis of gold films on germanium surfaces was carried out by the immersion of the germanium substrate in an aqueous gold salt solution at room temperature, as shown in Scheme 1. As is the case with all galvanic displacement reactions, the deposition process depends upon spontaneous redox reactions occurring between the semiconductor surface and the metal ions in the solution. As a result of the sufficiently high reduction potential of gold ions ($E°_{Au^{3+}}/Au^{\circ} = +1.42$ V vs NHE), the process leads to oxidation of the germanium surface that is supplying the electrons to reduce the gold ions to metallic gold on the surface, according to the following set of eqs 1 and 2 (29)

$$\text{Anodic: } Ge \rightarrow Ge^{4+} + 4e^{-} \quad E°_{Ge^{4+}/Ge} = 0.12 \text{ V vs NHE} \quad (1)$$

$$\text{Cathodic: } Au^{3+} + 3e^{-} \rightarrow Au°(s) \quad E°_{Au^{3+}/Au} = +1.42 \text{ V vs NHE} \quad (2)$$

The formation of a gold film on the surface of a Ge(111) wafer shard after 20 min immersion in 0.1 mM $KAuCl_4$(aq) at room temperature is shown in the plan view SEM image in Figure 1a. The germanium surface is covered with 3D gold islands of ~20 nm in thickness as revealed from the cross-sectional SEM image (Figure 1b). The oxidation of the germanium surface results in the formation of various forms of germanium oxide (GeO_2) that are water-soluble (68, 73, 74). In contrast with silicon, whose oxide requires the presence of a fluoride ion source to assist in its dissolution, studies of galvanic displacement on germanium have been carried out both in its presence (29) and absence (32, 33, 35, 36, 52, 53, 66, 67, 75). When galvanic displacement is carried out under the same conditions, but in the presence of 20% HF(aq), there are no significant differences in film thickness and morphology (compare SEM images a and b with c and d in Figure 1). Even higher concentrations of HF(aq) of 40% look similar, as shown in the Supporting Information. Thus by SEM analysis, the conclusion would be that HF has little effect on the metallization of germanium, under these conditions.

Although SEM is understandably the most commonly used method for characterization (48, 49, 76–83), it can be deceptive as is found in this work; seemingly similar metal-on-semiconductor films (by SEM) may have very different crystallinities and relative orientations (vide infra). As a result, it is critical to understand the growth of the metallic films with regards to their crystallinity (are they amorphous, or poly- and single crystalline?) and to investigate the interfacial characteristics (crystal orientation, film texture, composition of the metal-semiconductor interface, etc) by complementary means (84, 85). In this work, we describe the use of a number of different X-ray diffraction (XRD) analyses, as well as high-resolution TEM and nanobeam (~5 nm) selected area electron diffraction (SAED) imaging to better illuminate the nature of these films.

Although well-known to the reader, a schematic diagram of the experimental XRD setup is shown (Figure 2) to clearly define the various angles that will be manipulated to produce two-dimensional (2D) frames, pole figures, $\theta-2\theta$ scans and rocking curves for data obtained from a series of gold-on-germanium samples prepared via galvanic displacement. When examining these samples via XRD, a 2D X-ray diffraction system is advantageous because it allows the acquisition of 2θ Bragg diffractions over a wide range of chi (χ) angles simultaneously (86, 87). Hence, a large fraction of diffraction rings is measured simultaneously, important for samples with a preferred orientation and texture, and therefore yielding more information than one-dimensional sampling (86, 87). Figure 3a–i represents the XRD 2D frames, acquired while probing the films out-of-plane orientation by $\theta-2\theta$ scans, for gold-on-germanium samples prepared under similar conditions, varying only the concentration of HF(aq). The samples were prepared by immersing

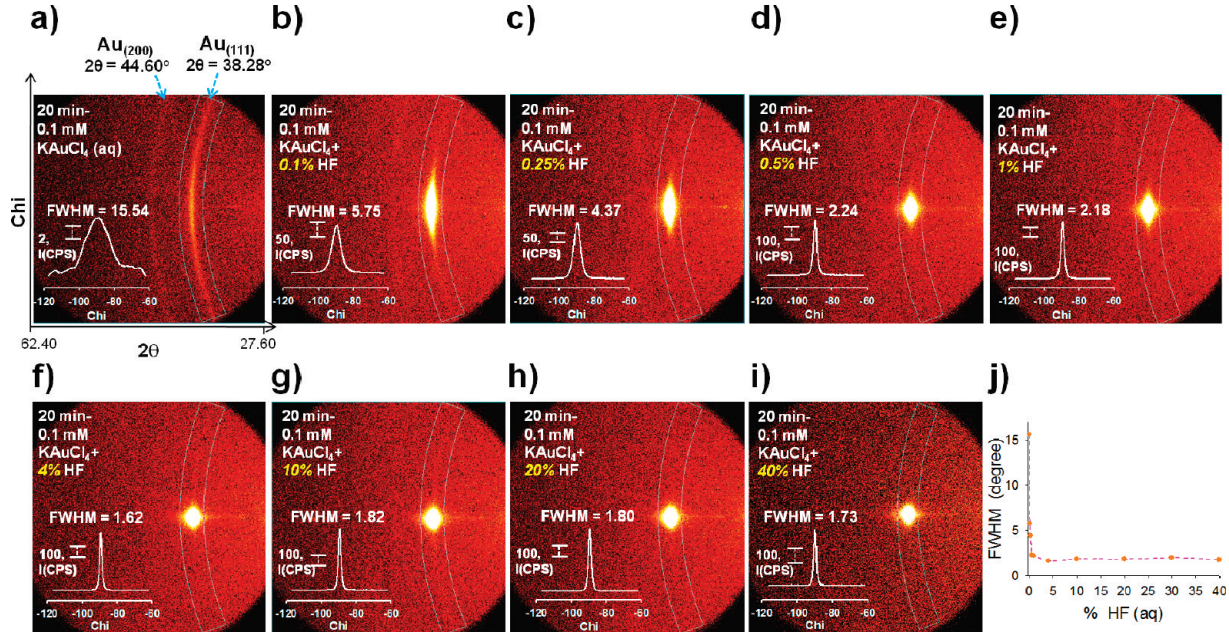

FIGURE 3. XRD 2D frames obtained for gold galvanically displaced on germanium surfaces. The gold films are formed after a 20 min immersion of Ge(111) shards in 0.1 mM $KAuCl_4$(aq) + x% of HF(aq); (a) $x = 0$, (b) $x = 0.1$, (c) $x = 0.25$, (d) $x = 0.5$, (e) $x = 1$, (f) $x = 4$, (g) $x = 10$, (h) $x = 20$, and (i) $x = 40$. The inset white peaks show the ($I-\chi$) plots, representing the diffraction intensities at $2\theta = 38.28°$, Au(111), along with chi (χ). (j) Plot shows the change of the fwhm values of the ($I-\chi$) peaks with HF concentrations.

a Ge(111) substrate for 20 min in 0.1 mM $KAuCl_4$(aq) at room temperature and increasing the concentration of HF(aq) from 0 to 40%. Within the 2D frame, diffraction patterns from different families of gold planes diffracting in the 2θ range of 27.6−62.4° are shown. The expected diffraction from a family of planes of a polycrystalline film with random orientation would show uniformly distributed intensity along the Debye diffraction ring (88). Localized high-intensity patterns of spots located along the ring, however, are diffractions that result from a preferred orientation of the gold film (88) (vide infra).

As can be seen from Figure 3a−i, there is an obvious effect of HF(aq) concentration over the range of 0−40%, based upon the XRD 2D frame analyses for gold-on-germanium. Starting with the case of 0% HF(aq), shown in Figure 3a, two Debye diffraction rings are observed at $2\theta =$ 38.28 and 44.60° that correspond to Au(111) and Au(200) planes, respectively (89). The Au(111) ring is of higher intensity than the Au(200) ring. Moreover, the intensity of the Au(111) ring is not uniformly distributed and is somewhat concentrated toward the center as shown in the inset for the intensity versus χ plot (fwhm = 15.54°), pointing to some degree of orientation of the grown gold film (having some fiber texture). The presence of even low concentrations of HF(aq) results in the obvious transformation of the Debye diffraction patterns from rings into spots, indicating the formation of a highly ordered (textured) gold film.

The inset (intensity−χ) peaks in Figure 3 represent plots of the diffraction intensity at $2\theta = 38.28°$, the Au(111) plane, versus χ. The fwhm of the inset plots can be used to represent the diffraction on the χ scale and to give an indication of the degree of orientation. When these fwhm measurements are plotted (Figure 3j) versus the % of HF(aq), it can be seen that the fwhm drops from 15.5° at 0% HF(aq) to 1.7° at 40% HF(aq), respectively. The greatest drop is seen from 0% HF(aq) to 0.1% (HF), indicating that even small amounts of HF(aq) are playing a critical role in the deposition process. Higher concentrations of HF(aq) do result in an increased tightening of the fwhm, but only to a small degree. Because a small fwhm within the intensity−χ plots reveals a greater degree of ordering of the Au(111) planes with respect to the Ge(111) surface plane, it can be seen that HF(aq) is involved in ordering of the metallization on the germanium surface.

XRD $\theta-2\theta$ scans probing the out-of-plane orientation of the grown gold film, shown in Figure 4, are observed by integrating the intensity of diffraction patterns observed from diffraction frames covering a 2θ scale in the range of 2.5−112°, acquiring diffractions from all gold planes. In the absence of HF(aq), with 0.1 mM $KAuCl_4$(aq) (Figure 4a), five peaks are observed for Au on Ge(111) at $2\theta = 38.28$, 44.60, 64.80, 77.63, and 82.35°, which correspond to Au(111), Au(200), Au(220), Au(311), and Au(222), respectively (89). The intensity ratio of Au(111) to Au(200) planes is 11.80, which is about 1 order of magnitude greater than the value of 1.33 observed for powder diffraction (JCPDS tables) (89). The high intensity ratio points to the oriented nature of the gold film on the germanium surface (fiber textured): The gold film has grown with a large fraction of (111) planes parallel to the Ge(111) surface. When 0.1% HF(aq) is added to the deposition solution of 0.1 mM $KAuCl_4$(aq), the Au(220) and Au(311) peaks vanish, leaving only the Au(111), Au(200), and Au(222) features (Figure 4b). In the case of HF(aq), concentrations higher than 0.25% (Figure 4c,d, and Figure S4 in the Supporting Information), the Au(200) peak disappears, leaving only the Au(111) and Au(222) peaks, indicating the formation of highly textured gold films on the germanium surfaces. To summarize, a Au(111)//Ge(111) out-

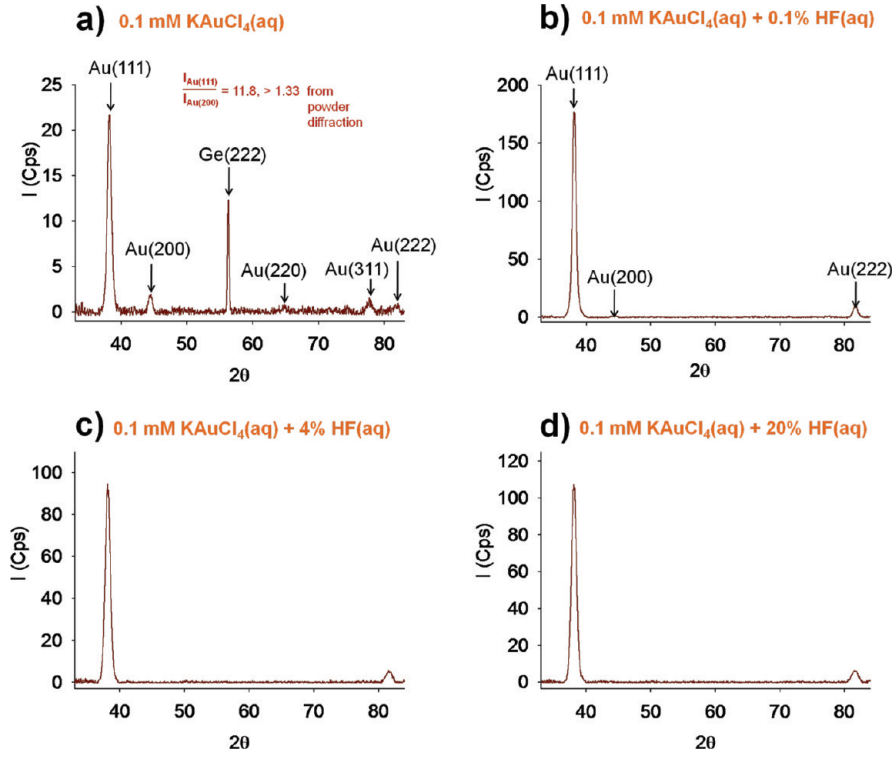

FIGURE 4. XRD $\theta-2\theta$ scans probing the out-of-plane orientation of gold films on Ge(111). The gold films were prepared after 20 min immersion of the germanium shards in a mixture of 0.1 mM $KAuCl_4$(aq) + x% of HF(aq); (a) $x = 0$, (b) $x = 0.1$, and (c) $x = 4$, and (d) 20% HF(aq).

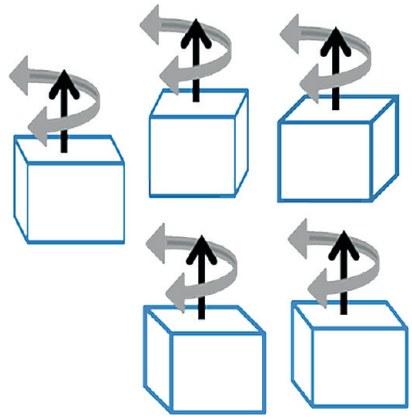

FIGURE 5. Schematic of fiber textured crystals. The grains are aligned along the vertical (black) texture axis, whereas they are randomly oriented in the azimuthal direction (gray) around the texture axis.

of-plane orientation relationship is obvious in all the gold-on-germanium samples, but those with greater concentrations of HF(aq) are clearly more highly textured.

Although it may be stated that the out-of-plane ⟨111⟩ crystallographic directions of most of the gold film crystallites are aligned parallel to the surface normal (texture axis), the crystalline orientation may (or may not) be randomly distributed in the azimuthal direction (in-plane orientation, vide infra), as shown schematically in Figure 5 (90). Fiber texture crystallites are characterized by their one degree of orientational freedom, which is the angle of rotation around the texture axis (Figure 5) (85). Further proving the fiber texture nature of the gold film grown on Ge(111) from aqueous gold salt deposition bath requires investigating the in-plane orientation of the Au crystallites. Pole figure analysis provides in-plane information by collecting the diffraction intensities while rotating a sample azimuthally 360° along the rotation angle (Φ) at different tilting angles (χ), and setting 2θ constant at the value for the plane of interest (Figure 2) (85). Pole figures can differentiate between the three types of texture: random, fiber, and epitaxial. These three textures result in featureless pole figures, a ring pattern surrounding the pole figure central point, and defined spots at certain (Φ, χ) positions on the pole figure, respectively (91). Panels a and b in Figure 6 show the germanium (111) surface and contour pole figures, respectively, which were obtained by setting $2\theta = 27.31°$ for the (111) planes of germanium single crystal substrate and acquiring Bragg diffractions while rotating the sample along the substrate in-plane "azimuthal" direction at different tilting chi angles. In these figures, the spot (peak) observed at $\chi = 0°$ corresponds to diffractions acquired from the Ge {111} planes parallel to the substrate surface. At $\chi = 70.5°$, the observed three equally spaced ($\Delta\Phi = 120°$) diffractions spots (peaks) arise from the next set of (111) reflections in the face-centered cubic (fcc) crystal structure. The locations of the three peaks agree with the calculated $\chi = 70.5°$ that corresponds to the angle between the (111) plane and each of the $(\bar{1}11)$, $(1\bar{1}1)$, and $(11\bar{1})$ planes in the cubic system (see Figure 7).

The (111) Au pole figures for a gold film grown after 20 min immersion of the germanium substrate in 0.1 mM $KAuCl_4$(aq) in absence of HF(aq) are shown in panels c and d in Figure 6, which were acquired by setting $2\theta = 38.28°$ for Au(111). The diffraction peak observed at $\chi = 0°$, Figure 6c, indicates that the ⟨111⟩ directions of the gold grains are aligned normal to the substrate surface. The ring diffraction

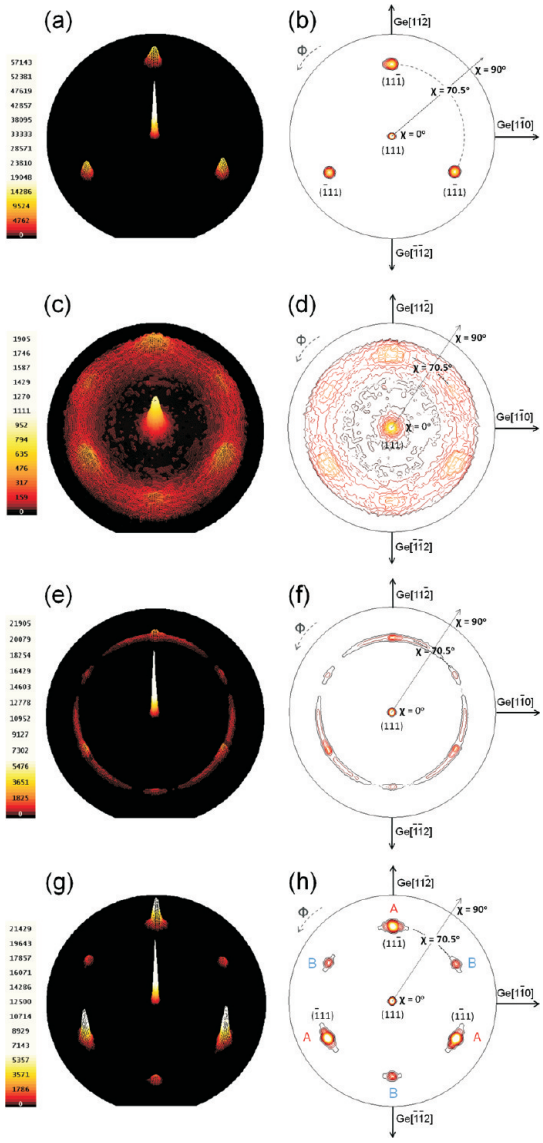

FIGURE 6. X-ray (111) pole figures for (a, b) an unfunctionalized Ge(111) substrate, and (c–h) gold films on Ge(111) substrates, produced after 20 min immersion of the germanium substrates in 0.1 mM $KAuCl_4$(aq) + x % HF(aq). The specific values of x are: (c, d) x = 0, (e, f) x = 4, and (g, h) x = 20. The (111) surface and contour pole figures are represented in (a, c, e, g) and (b, d, f, h), respectively. The pole figures were obtained by setting 2q equals to the angle of diffraction from the (111) planes ($2\theta = 27.31$ and 38.28° for Ge and Au, respectively) and collecting the diffraction intensity while rotating the sample azimuthally at different tilting angles (χ).

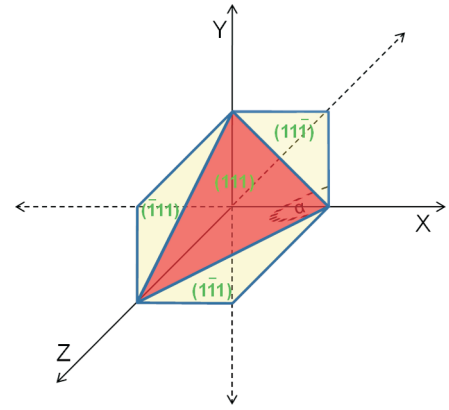

FIGURE 7. Schematic of the (111), ($\bar{1}$11), (1$\bar{1}$1), and (11$\bar{1}$) planes of face-centered cubic (fcc) structure. The angle α = 70.5° representing the angle between the (111) plane and each of the ($\bar{1}$11), (1$\bar{1}$1), and (11$\bar{1}$) planes in the cubic system.

pattern at $\chi = 70.5°$ reveals diffraction from gold grains that are oriented randomly in the azimuthal, in-plane, direction (meaning that it is a fiber textured gold film as shown schematically in Figure 5). The pole figure analysis is a confirmation of the fiber texture behavior indicated from the θ–2θ scan in Figure 4a, and the diffraction pattern in Figure 3a. The θ–2θ scans shown earlier (Figure 4c,d) of the gold films grown from reaction mixtures containing 4 and 20 % HF(aq) and 0.1 mM $KAuCl_4$(aq) show diffractions from only Au(111) and Au(222), and there is no apparent difference in the out-of-plane information observed in either set of conditions. The pole figures can, however, help to extract more information regarding the gold-on-germanium film orientation, and in fact, show that these interfaces differ quite substantially. While investigating the in-plane orientation of a gold film grown from a solution containing 4 % HF(aq) along with 0.1 mM $KAuCl_4$(aq), the pole figure diffraction patterns (Figure 6e, f) indicate minor in-plane disorder as revealed from the less dimensioned ring pattern at $\chi = 70.5°$. In the presence of 20 % HF(aq), along with the gold salt solution in the reaction mixture, well-defined diffraction spots and peaks are observed at $\chi = 70.5°$ as shown in panels g and h in Figure 6. The sharpness of the Au(111) diffractions and the "clean" pole figure indicate a higher degree of alignment in the azimuthal direction, suggestive of an epitaxial gold film. The six peaks observed in Figure 6g also suggest that there are two types of epitaxy or in-plane textures for the Au/Ge(111) system. By convention, these are denoted as "A" and "B", with A peaks appearing at the same azimuthal positions as those of the Ge substrate in Figure 6a, whereas B orientation is rotated 180° relative to A with an intensity equal to ~1/5 of that of A. Hence, in the case of the A orientation, all the crystallographic directions of the gold film are coincident with those of the germanium substrate, whereas in the case of the B orientation, the film structure is rotated 180° relative to the germanium structure. A similar A–B orientation has been observed for evaporated silver (92) and sputtered copper (93) films on silicon surfaces. As determined from the pole figure shown in Figure 6h, the two epitaxial relationships for the A and B in-plane orientations are Au(111)[11$\bar{2}$]// Ge(111)[11$\bar{2}$], and Au(111)[$\bar{1}$1$\bar{2}$]//Ge(111)[11$\bar{2}$], respectively. Noticeably, in panels c and d in Figure 6, these two "A and B" in-plane orientations appear to have only slight preferred alignment of all the possible random in-plane orientations.

The concept of mosaicity has been used to describe the ideality of single crystals (85). Single crystals are considered as small building blocks that extend in a nonperfect periodicity from one side of the crystal to the other; exhibit variation in orientation along the sample reference plane. In the case of epitaxial film–substrate systems, mosaicity is a result of large lattice mismatch and relaxation that can cause tilted grains or deviated orientation of the grains along the out-of-plane direction (85). The out-of-plane mosaicity of the gold films on germanium was determined by an X-ray

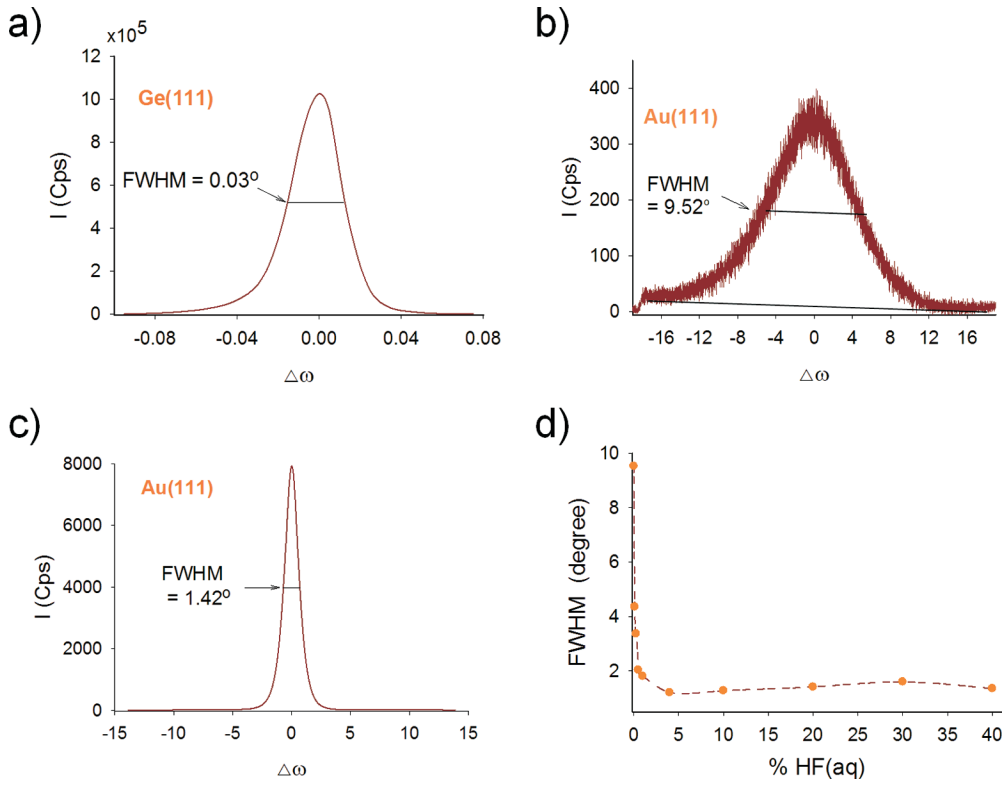

FIGURE 8. X-ray rocking curves for (a) Ge(111) substrate, (b) Au(111) from gold films prepared after 20 min immersion of germanium substrate in 0.1 mM $KAuCl_4$(aq), and (c) in a mixture of 0.1 mM $KAuCl_4$ + 20% HF(aq). (d) Plot shows the effect of HF(aq) concentration on the fwhm of the rocking curves.

rocking curve. Out-of-plane mosaicity can be investigated from rocking curves acquired by fixing the detector position at the required 2θ of the plane of interest (usually the plane with the same *hkl* out-of-plane direction) and rocking the sample along the ω axis (Figure 2). Figure 8 shows the X-ray rocking curves of a Ge(111) substrate (Figure 8a, 2θ was fixed at 27.31°), and Au(111) from gold films on Ge(111). Panels b and c in Figure 8 correspond to deposition solutions of 0.1 mM $KAuCl_4$(aq) in the absence of HF(aq), and in the presence of 20% HF(aq), respectively; in both panels b and c, 2θ was fixed at 38.28°. The mosaic spread was determined from the full width at half-maximum (fwhm) of the rocking curves. The fwhm of gold films grown in the presence and in the absence of 20% HF(aq) are 1.42 and 9.52°, respectively, compared to 0.03° for the germanium substrate. A plot summarizing the change in the fwhm or the mosaic spread of the gold film as a function of increasing HF(aq) concentrations is shown in Figure 8d. As can be clearly seen, HF(aq) is required for more ordered structures, with a lower mosaic spread, and may be due to the simultaneous etching of the germanium oxide products formed during the galvanic displacement processes, leading to better direct gold–germanium contact. This improved contact between the growing gold film and the underlying germanium could lead to better transfer of crystallographic "information" from the germanium to the nucleating and growing gold film, leading to a higher degree of alignment.

To confirm the epitaxial relationship between germanium and gold film, we harnessed the precision of transmission electron microscopy (TEM) nanobeam diffraction analyses to characterize the nature of gold–germanium interface formed via the galvanic displacement process. Figure 9a shows cross-sectional high-resolution TEM image for a gold epilayer, on flat single crystal Ge(111), prepared by the immersion of germanium substrate in a mixture of 0.1 mM $KAuCl_4$(aq) and 20% HF(aq) for 20 min. Nanobeam diffraction (beam size ~5 nm) patterns were taken along the $[\bar{1}12]$ zone axis from three different locations, as shown in Figure 9a: "1" marks the location on the germanium substrate, "2" indicates the gold–germanium interface, and "3" corresponds to the gold layer. The nanobeam diffraction patterns taken at these three spots are shown in Figure 9b–d. The common viewing direction "$[\bar{1}12]$" for the diffraction patterns taken from both the germanium substrate (Figure 9b) and the top gold layer (Figure 9c), is indicative of the alignment of the gold layer with the underlying germanium substrate. The diffraction pattern from the Au–Ge interface, Figure 9d, shows that along the $[\bar{1}12]$ zone axis, every Bragg diffraction spot from the germanium has a corresponding gold spot with the identical orientation. The germanium pattern consists of spots, due to its single-crystal nature, arising from diffraction from the $(\bar{1}1\bar{1})$, (220), and $(13\bar{1})$ planes; gold shows diffraction from these same planes. Other features of note include the alignment of the {112} family of crystallographic planes, of both the germanium substrate and the gold overlayer. The gold $(\bar{1}1\bar{1})$ and (220) planes are parallel to the germanium $(\bar{1}1\bar{1})$ and (220) planes, respectively: $Au(\bar{1}1\bar{1})//Ge(\bar{1}1\bar{1})$ and Au(110)//Ge(110). Hence, the nanobeam diffraction patterns from gold film on germanium substrate are strongly indicative of the Au(111)-

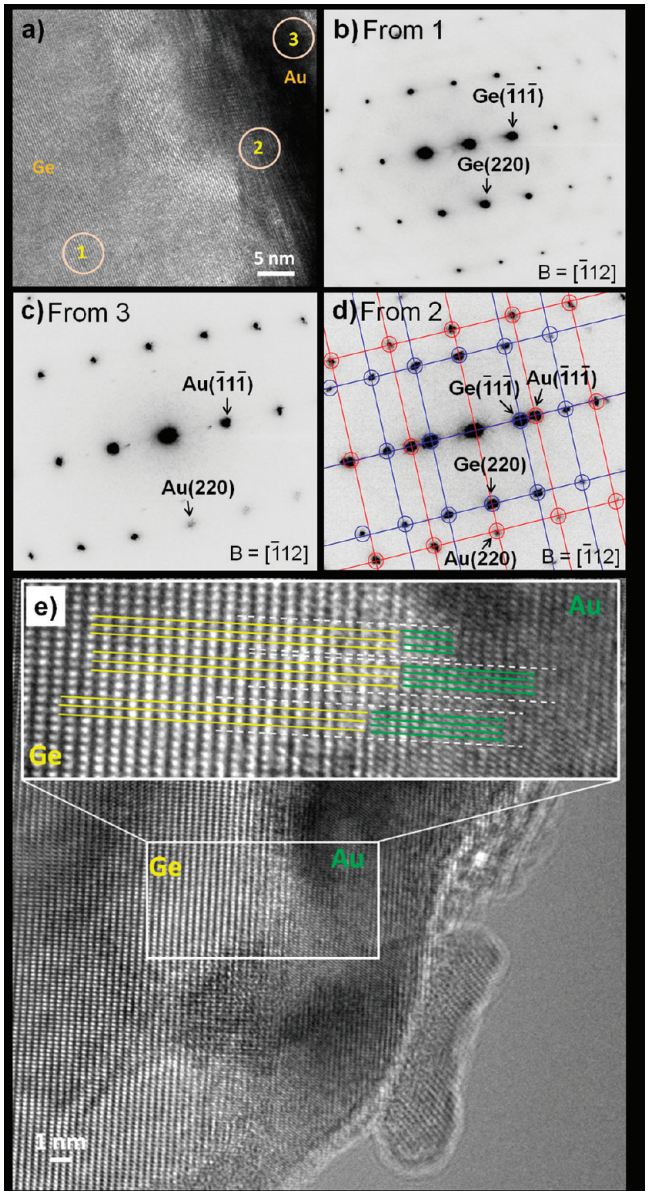

FIGURE 9. (a) Cross-sectional high-resolution transmission electron micrograph for a gold film on Ge(111), formed by immersing the germanium substrate in 0.1 mM $KAuCl_4$(aq) + 20% HF(aq) for 20 min. (b–d) Nanobeam diffraction patterns (probe ≈5 nm) taken along the [1̄12] zone axis from three different areas: (b) from germanium substrate (area marked 1 in image a), (c) from top gold area marked by 3 in image a, and (d) from the gold–germanium interfacial area marked by 2 in image a. Red and blue lines correspond to gold and germanium planes, respectively. (e) Cross-sectional HRTEM images, for gold–germanium interface, taken close to the [110] zone axis. The yellow and green lines show the coincident site lattice interfaces for the germanium and gold planes, respectively. The white lines show the alignment and the parallel nature of the gold epilayer to the underlying germanium substrate.

[1̄12]//Ge(111)[1̄12] in-plane epitaxial relationship, which agrees with the epitaxial relationship observed from the XRD pole figure (vide supra, Figure 6g,h).

The phenomenon of heteroepitaxial crystallization involves the epitaxial growth of one layer (an epilayer) with a chemical composition and, typically, structural parameters different from those of the substrate (94). Lattice mismatch or misfit (the disregistry of the interfacial atomic arrangement of the substrate and the overgrown epilayer) is known to have a significant effect on epitaxy (94). Au(111) and Ge(111) with interplanar *d* spacings of 2.355 Å and 3.266 Å, respectively, have about a 27.9% lattice mismatch. By considering the coincident site lattice interface (CSL), however, in which three germanium lattices match with four gold lattices, $4xd_{Au(111)} = 9.42$ Å and $3xd_{Ge(111)} = 9.80$ Å, the lattice mismatch is only 3.8%, which may explain the reason for the heteroepitaxial growth of gold on germanium (Figure 9e). A CSL interface is most likely present for the epitaxial growth of galvanically displaced gold (49), and electron-beam evaporated gold (57) and silver (95) on Si(111) surfaces.

The final question that requires an explanation is the fundamental role of fluoride ion on the galvanic displacement process—what role does it play in the observed heteroepitaxial gold-on-germanium films? As mentioned earlier, the Ge(IV) oxides (the soluble forms of GeO_2, Scheme 1), formed during the corrosion half of the galvanic displacement reaction are water-soluble, but the suboxides, GeO_x ($x < 2$), are not. In the presence of HF(aq), however, both the Ge(IV) oxides and the suboxides are soluble (69, 70). It could be anticipated, therefore, that the presence of the suboxides hinders direct contact between the forming metallic gold and the germanium surface, leading to a less ordered (less textured) structure. A "cleaner" interface, as would be expected in the presence of HF(aq), with all oxides being continually stripped away as they are formed, however, must be leading to better contact, and hence a greater chance for heteroepitaxy between the gold and the germanium.

CONCLUSIONS

Galvanic displacement of germanium surfaces from aqueous solutions of gold salts resulted in oriented (fiber textured) gold films. The addition of higher concentrations of HF(aq) to the reaction mixture resulted in gold films with more ordered in-plane orientations that can be described as epitaxial in nature. The epitaxial behavior was further proved by cross-sectional TEM investigation involving nanobeam diffraction analyses. The epitaxial relationship observed from the pole figure analyses agrees with what was observed from the nanobeam diffraction pattern; Au(111)[1̄12]// Ge(111)[1̄12]. The epitaxy or the direct Au–Ge contact was further substantiated by high-resolution TEM analysis showing the coincident site lattice interface, in which four gold lattices coincident with three of germanium.

Acknowledgment. This work was supported by NSERC, the National Research Council of Canada (NRC-NINT), the University of Alberta, Alberta Ingenuity (Fellowship to SYS), and the Canada Research Chairs Program (CRC to JMB). We are also thankful for the technical support at NINT and the Alberta Centre for Surface Engineering and Science (ACSES). We thank to Mr. Jon Giencke from of Bruker AXS for assistance with X-ray diffraction and pole figure measurements. We thank Peng Li for his effort in preparing the TEM sample and his careful TEM imaging. We thank Mr. Steve Launspach from Surface Characterization Laboratories NRC National Institute for Nanotechnology for his valuable discussions and help. S.Y.S. thanks Cairo University, Egypt, for

his leave of absence to perform his Ph.D. studies at the University of Alberta.

Supporting Information Available: Additional SEM and XRD data for gold-functionalized interfaces (PDF). This material is available free of charge via the Internet at http://pubs.acs.org

REFERENCES AND NOTES

(1) Northrop, D. C. *Nature* **1980**, *284*, 403–404.
(2) Leong, M.; Doris, B.; Kedzierski, J.; Rim, K.; Yang, M. *Science* **2004**, *306*, 2057–2060.
(3) Wu, Y.; Xiang, J.; Yang, C.; Lu, W.; Lieber, C. M. *Nature* **2004**, *430*, 61–65.
(4) Li, B.; Luo, Z. Q.; Shi, L.; Zhou, J. P.; Rabenberg, L.; Ho, P. S.; Allen, R. A.; Cresswell, M. W. *Nanotechnology* **2009**, *20*.
(5) Ootsuka, T.; Liu, Z. X.; Osamura, M.; Fukuzawa, Y.; Otogawa, N.; Nakayama, Y.; Tanoue, H.; Makita, Y. *Mater. Sci. Eng., B* **2005**, *124*, 449–452.
(6) Giziewicz, W. P.; Fonstad, C. G. *J. Vac. Sci. Technol., A* **2002**, *20*, 1052–1056.
(7) Wang, Y.; Newaz, A. K. M.; Wu, J.; Solin, S. A.; Kavasseri, V. R.; Jin, N.; Ahmed, I. S.; Adesida, I. *Appl. Phys. Lett.* **2008**, *92*.
(8) Peng, K. Q.; Wang, X.; Lee, S. T. *Appl. Phys. Lett.* **2009**, *95*.
(9) Mokari, T.; Rothenberg, E.; Popov, I.; Costi, R.; Banin, U. *Science* **2004**, *304*, 1787–1790.
(10) Lin, K. W.; Chen, H. I.; Lu, C. T.; Tsai, Y. Y.; Chuang, H. M.; Chen, C. Y.; Liu, W. C. *Semicond. Sci. Technol.* **2003**, *18*, 615–619.
(11) Mieszawska, A. J.; Zamborini, F. P. *Chem. Mater.* **2005**, *17*, 3415–3420.
(12) Lin, H. H.; Gao, T.; Fantini, J.; Sailor, M. J. *Langmuir* **2005**, *21*, 1661–1661.
(13) Zamborini, F. P.; Smart, L. E.; Leopold, M. C.; Murray, R. W. *Anal. Chim. Acta* **2003**, *496*, 3–16.
(14) Huang, J. X.; Kim, F.; Tao, A. R.; Connor, S.; Yang, P. D. *Nat. Mater.* **2005**, *4*, 896–900.
(15) Shenhar, R.; Jeoung, E.; Srivastava, S.; Norsten, T. B.; Rotello, V. M. *Adv. Mater.* **2005**, *17*, 2206–2210.
(16) Park, J. I.; Lee, W. R.; Bae, S. S.; Kim, Y. J.; Yoo, K. H.; Cheon, J.; Kim, S. *J. Phys. Chem. B* **2005**, *109*, 13119–13123.
(17) Foster, E. W.; Kearns, G. J.; Goto, S.; Hutchison, J. E. *Adv. Mater.* **2005**, *17*, 1542–1545.
(18) McMillan, R. A.; Howard, J.; Zaluzec, N. J.; Kagawa, H. K.; Mogul, R.; Li, Y. F.; Paavola, C. D.; Trent, J. D. *J. Am. Chem. Soc.* **2005**, *127*, 2800–2801.
(19) El-Sayed, M. A. *Acc. Chem. Res.* **2001**, *34*, 257–264.
(20) Murphy, C. J.; Jana, N. R. *Adv. Mater.* **2002**, *14*, 80–82.
(21) Lee, K. S.; El-Sayed, M. A. *J. Phys. Chem. B* **2006**, *110*, 19220–19225.
(22) Mohamed, M. B.; Volkov, V.; Link, S.; El-Sayed, M. A. *Chem. Phys. Lett.* **2000**, *317*, 517–523.
(23) Leung, S.; Milnes, A. G.; Chung, D. D. L. *Thin Solid Films* **1983**, *104*, 109–131.
(24) Brenner, A.; Riddell, G. E. *J. Res. Natl. Bureau Stand.* **1946**, *37*, 31–34.
(25) Zhao, L. Y.; Siu, A. C. L.; Petrus, J. A.; He, Z. H.; Leung, K. T. *J. Am. Chem. Soc.* **2007**, *129*, 5730–5734.
(26) San Paulo, A.; Arellano, N.; Plaza, J. A.; He, R. R.; Carraro, C.; Maboudian, R.; Howe, R. T.; Bokor, J.; Yang, P. D. *Nano Lett.* **2007**, *7*, 1100–1104.
(27) daRosa, C. P.; Maboudian, R.; Iglesia, E. *J. Electrochem. Soc.* **2008**, *155*, E70−E78.
(28) Carraro, C.; Maboudian, R.; Magagnin, L. *Surf. Sci. Rep.* **2007**, *62*, 499–525.
(29) Magagnin, L.; Maboudian, R.; Carraro, C. *J. Phys. Chem. B* **2002**, *106*, 401–407.
(30) Aizawa, M.; Buriak, J. M. *Chem. Mater.* **2007**, *19*, 5090–5101.
(31) Aizawa, M.; Buriak, J. M. *J. Am. Chem. Soc.* **2006**, *128*, 5877–5886.
(32) Aizawa, M.; Cooper, A. M.; Malac, M.; Buriak, J. M. *Nano Lett.* **2005**, *5*, 815–819.
(33) Aizawa, M.; Buriak, J. M. *J. Am. Chem. Soc.* **2005**, *127*, 8932–8933.
(34) Nezhad, M. R. H.; Aizawa, M.; Porter, L. A.; Ribbe, A. E.; Buriak, J. M. *Small* **2005**, *1*, 1076–1081.
(35) Porter, L. A.; Choi, H. C.; Schmeltzer, J. M.; Ribbe, A. E.; Elliott, L. C. C.; Buriak, J. M. *Nano Lett.* **2002**, *2*, 1369–1372.
(36) Porter, L. A.; Choi, H. C.; Ribbe, A. E.; Buriak, J. M. *Nano Lett.* **2002**, *2*, 1067–1071.
(37) Niwa, D.; Homma, T.; Osaka, T. *J. Phys. Chem. B* **2004**, *108*, 9900–9904.
(38) Gorostiza, P.; Allongue, P.; Diaz, R.; Morante, J. R.; Sanz, F. *J. Phys. Chem. B* **2003**, *107*, 6454–6461.
(39) Sun, Y. G.; Wiederrecht, G. P. *Small* **2007**, *3*, 1964–1975.
(40) Sun, X. H.; Wong, N. B.; Li, C. P.; Lee, S. T.; Kim, P. S. G.; Sham, T. K. *Chem. Mater.* **2004**, *16*, 1143–1152.
(41) Ye, X. R.; Wai, C. M.; Zhang, D. Q.; Kranov, Y.; McIlroy, D. N.; Lin, Y. H.; Engelhard, M. *Chem. Mater.* **2003**, *15*, 83–91.
(42) Lv, S.; Suo, H.; Zhou, T. L.; Wang, C. X.; Jing, S. Y.; Fu, Q. B.; Xu, Y. A.; Zhao, C. *Solid State Commun.* **2009**, *149*, 227–230.
(43) Gao, D.; He, R. R.; Carraro, C.; Howe, R. T.; Yang, P. D.; Maboudian, R. *J. Am. Chem. Soc.* **2005**, *127*, 4574–4575.
(44) Niwa, D.; Homma, T.; Osaka, T. *J. Electrochem. Soc.* **2005**, *152*, C54–C59.
(45) Lin, H. H.; Mock, J.; Smith, D.; Gao, T.; Sailor, M. J. *J. Phys. Chem. B* **2004**, *108*, 11654–11659.
(46) Peng, K. Q.; Zhu, J. *J. Electroanal. Chem.* **2003**, *558*, 35–39.
(47) Oskam, G.; Long, J. G.; Natarajan, A.; Searson, P. C. *J. Phys. D: Appl. Phys.* **1998**, *31*, 1927–1949.
(48) Sayed, S. Y.; Daly, B.; Buriak, J. M. *J. Phys. Chem. C* **2008**, *112*, 12291–12298.
(49) Sayed, S. Y.; Wang, F.; Mallac, M.; Meldrum, A.; Egerton, R. F.; Buriak, J. M. *ACS Nano* **2009**, *3*, 2809–2817.
(50) Yasseri, A. A.; Sharma, S.; Jung, G. Y.; Kamins, T. I. *Electrochem. Solid-State Lett.* **2006**, *9*, C185–C188.
(51) Warren, S.; Reitzle, A.; Kazimirov, A.; Ziegler, J. C.; Bunk, O.; Cao, L. X.; Renner, F. U.; Kolb, D. M.; Bedzyk, M. J.; Zegenhagen, J. *Surf. Sci.* **2002**, *496*, 287–298.
(52) Zhang, J. G.; Gao, Y.; Hanrath, T.; Korgel, B. A.; Buriak, J. M. *Chem. Commun.* **2007**, 1438–1440.
(53) Brejna, P. R.; Griffiths, P. R.; Yang, J. *Appl. Spectrosc.* **2009**, *63*, 396–400.
(54) Piscopiello, E.; Tapfer, L.; Antisari, M. V.; Paiano, P.; Prete, P.; Lovergine, N. *Phys. Rev. B* **2008**, *78*, 0353051−0353057.
(55) Sato, K.; Huang, W. J.; Bohra, F.; Sivaramakrishnan, S.; Tedjasaputra, A. P.; Zuo, J. M. *Phys. Rev. B* **2007**, *76*, 144113−1144113−8.
(56) Arakaki, H.; Ohashi, K.; Sudou, T. *Semicond. Sci. Technol.* **2004**, *19*, 127–132.
(57) Yokota, Y.; Hashimoto, H.; Saito, N.; Endoh, H. *Jpn J Appl Phys., Part 2* **1986**, *25*, L168–L170.
(58) Shimizu, T.; Xie, T.; Nishikawa, J.; Shingubara, S.; Senz, S.; Gosele, U. *Adv. Mater.* **2007**, *19*, 917–920.
(59) Shimizu, T.; Senz, S.; Shingubara, S.; Gosele, U. *Appl. Phys. A: Mater. Sci. Process.* **2007**, *87*, 607–610.
(60) Murarka, S. P. *Metallization: Theory and Practice for VLSI and ULSI*; Butterworth-Heineman: Stoneham, MA, 1992.
(61) Chao, Y. L.; Scholz, R.; Reiche, M.; Gosele, U.; Woo, J. C. S. *Jpn. J. Appl. Phys., Part 1* **2006**, *45*, 8565–8570.
(62) Nayfeh, A.; Chui, C. O.; Saraswat, K. C.; Yonehara, T. *Appl. Phys. Lett.* **2004**, *85*, 2815–2817.
(63) Greytak, A. B.; Lauhon, L. J.; Gudiksen, M. S.; Lieber, C. M. *Appl. Phys. Lett.* **2004**, *84*, 4176–4178.
(64) Sze, S. M. *Physics of Semiconductor Devices*; Wiley: New York, 1981.
(65) Bojarczuk, N. A.; Copel, M.; Guha, S.; Narayanan, V.; Preisler, E. J.; Ross, F. M.; Shang, H. *Appl. Phys. Lett.* **2003**, *83*, 5443–5445.
(66) Lee, K. Y.; Han, S. W.; Choi, H. C. *Bull. Korean Chem. Soc.* **2009**, *30*, 3113–3116.
(67) Bravo-Vasquez, J.-P.; Fenniri, H. *J. Phys. Chem. C* **2009**, *113*, 12897–12900.
(68) Park, K.; Lee, Y.; Lee, J.; Lim, S. *Appl. Surf. Sci.* **2008**, *254*, 4828–4832.
(69) Rivillon, S.; Chabal, Y. J.; Amy, F.; Kahn, A. *Appl. Phys. Lett.* **2005**, *87*, 253101.
(70) Benoit, R. L.; Place, J. *Can. J. Chem.* **1963**, *41*, 1170–&.
(71) Okumura, H.; Akane, T.; Matsumoto, S. *Appl. Surf. Sci.* **1998**, *125*, 125–128.
(72) Akane, T.; Tanaka, J.; Okumura, H.; Matsumoto, S. *Appl. Surf. Sci.* **1997**, *108*, 303–305.
(73) Murthy, M. K.; Hill, H. *J. Am. Ceram. Soc.* **1965**, *48*, 109–&.
(74) Vekhov, V. A.; Vitukhnovskaya, B. S.; Doronkina, R. F. *Izv. Vyssh. Uchebn. Zaved., Khim. Khim. Tekhnol.* **1964**, *7*, 1018–19.

(75) Johnson, M.; Kelly, J. A.; Henderson, E. J.; Veinot, J. G. C. *IOP Conf. Ser.: Mater. Sci. Eng.* **2009**, *6*, 012031/1−012031/5.
(76) Jim, S. R.; Taschuk, M. T.; Morlock, G. E.; Bezuidenhout, L. W.; Schwack, W.; Brett, M. J. *Anal. Chem.* **2010**, *82*, 5349–5356.
(77) Liu, C.; Shields, P. A.; Denchitcharoen, S.; Stepanov, S.; Gott, A.; Wang, W. N. *J. Cryst. Growth* **2007**, *300*, 104–109.
(78) McClure, S. A.; Worfolk, B. J.; Rider, D. A.; Tucker, R. T.; Fordyce, J. A. M.; Fleischauer, M. D.; Harris, K. D.; Brett, M. J.; Buriak, J. M. *ACS Appl. Mater. Interfaces* **2010**, *2*, 219–229.
(79) Mizuno, H.; Buriak, J. M. *ACS Appl. Mater. Interfaces* **2009**, *1*, 2711–2720.
(80) Krause, K. M.; Taschuk, M. T.; Harris, K. D.; Rider, D. A.; Wakefield, N. G.; Sit, J. C.; Buriak, J. M.; Thommes, M.; Brett, M. J. *Langmuir* **2010**, *26*, 4368–4376.
(81) Brett, M. J.; Hawkeye, M. M. *Science* **2008**, *319*, 1192–1193.
(82) Hawkeye, M. M.; Brett, M. J. *J. Vac. Sci. Technol., A* **2007**, *25*, 1317–1335.
(83) Teki, R.; Parker, T. C.; Li, H. F.; Koratkar, N.; Lu, T. M.; Lee, S. *Thin Solid Films* **2008**, *516*, 4993–4996.
(84) Brundle, C. R.; Charles k Evans, J.; Wilson, S. *Encyclopedia of Materials Characterization: Surfaces, Interfaces, Thin Films*; Butterworth-Heinemann: Stoneham, MA, 1992.
(85) Birkholz, M. *Thin Film Analysis by X-Ray Scattering*; Wiley-VCH: Weinheim, Germany, 2006.
(86) Van Hest, M.; Leenheer, A. J.; Perkins, J. D.; Teplin, C. W.; Ginley, D. S. In *Conference Record of the 2006 IEEE 4th World Conference on Photovoltaic Energy Conversion*; IEEE: Piscataway, NJ, 2006; Vols *1* and *2*, pp 1368−1371.
(87) *General Area Detector Diffraction Systems User's Manual*; Bruker AXS: Madison, WI; version 4.
(88) Liew, S. L.; Balakrisnan, B.; Ho, C. S.; Thomas, O.; Chi, D. Z. *J. Electrochem. Soc.* **2007**, *154*, H9–H12.
(89) XX.
(90) Tang, F.; Parker, T.; Wang, G. C.; Lu, T. M. *J. Phys. D: Appl. Phys.* **2007**, *40*, R427–R439.
(91) Detavernier, C.; Ozcan, A. S.; Jordan-Sweet, J.; Stach, E. A.; Tersoff, J.; Ross, F. M.; Lavoie, C. *Nature* **2003**, *426*, 641–645.
(92) Park, K. H.; Smith, G. A.; Rajan, K.; Wang, G. C. *Metall. Trans., A* **1990**, *21*, 2323–2332.
(93) Jiang, H.; Klemmer, T. J.; Barnard, J. A.; Doyle, W. D.; Payzant, E. A. *Thin Solid Films* **1998**, *315*, 13–16.
(94) Herman, M. A., Richter, W. & Sitter, H. *Epitaxy: Physical Principles and Technical Implementation*; Springer: New York, 2004.
(95) Li, B. Q.; Zuo, J. M. *Surf. Sci.* **2002**, *520*, 7–17.

AM100698W